Available online at www.sciencedirect.com
SCIENCE DIRECT
Cement & Concrete Composites 28 (2006) 337–348
Cement & Concrete Composites
www.elsevier.com/locate/cemconcomp

Use of surface waves and seismic refraction for the inspection of circular concrete structures

Julien Lagarde [a], Odile Abraham [a,*], Laurent Laguerre [a], Philippe Côte [a], Jack-Pierre Piguet [b], Cyrille Balland [c], Gilles Armand [b]

[a] LCPC, Division Reconnaissance et Mécanique des sols, BP4129, 44341 Bouguenais Cedex, France
[b] ANDRA, Laboratoire souterrain de recherches Meuse/Haute-Marne, BP9, 55290 Bure, France
[c] INERIS, Ecole des Mines de Nancy, 54042 Nancy Cedex, France

Abstract

In this paper, the propagation of both longitudinal and surface waves will be investigated within the scope of seismic measurements recorded along the circumference of concave structures. The underlying objective herein is to recover, in a non-destructive manner, the mechanical material properties from seismic refraction as well as multiple-channel analysis of surface wave measurements. This experimental set-up along the circumference is currently employed in the case of circular concrete tunnels or shafts when sensors cannot be installed along the structural baseline. The influence of curvature on longitudinal wave propagation will first be quantified by means of a simple analytical model. If curvature is neglected, the thickness of a damaged concrete cover will be overestimated, whereas its longitudinal wave propagation velocity will be underestimated. For surface waves, it will be shown that the influence of curvature exerts a major impact on phase velocity, which cannot be incorporated into the classical multiple-channel analysis of the surface wave forward problem. Consequently, we have developed a numerical model dedicated to such geometries that relies upon complex values of the surface wave phase velocity. The first part of this article is dedicated to the description of the mathematical derivation of the propagation of surfaces wave in a curved medium. This numerical model is then compared with experimental data recorded on a reduced-scale concrete tunnel of metric size. The agreement between experimental and numerical results, as well as seismic refraction and the multiple-channel analysis of surface wave complementarity, form the basis of an in situ, non-destructive testing technique.

Keywords: Surface waves; Seismic refraction; Semi-analytical models; Dispersion curve; Concrete; Reduced-scale models

1. Introduction

The mechanical characterization of the first few centimeters may be undertaken by various pinpoint destructive or semi-destructive tests [7]; these provide precise, albeit very localized, information. One advantage of the Non-Destructive Evaluation (NDE) approach is to offer a possible extensive view of the structure through mapping as well as periodic surveying. Even though NDE results consist of a physical parameter not directly linked to the set of parameters that structural engineers require [6], the seismic waves can provide information on mechanical properties at a very low strain level. Such information proves relevant in determining the judicious positioning of destructive or semi-destructive tests and/or eventually ascertaining an extrapolation between them. The objective behind the seismic method is to replicate the mechanical characteristic of the concrete as a function of depth. A variation in the mechanical moduli of concrete, e.g. a decrease in case of damage, will indeed correspond to a decrease in the longitudinal/compression (c_L) and transverse/shear (c_T) wave velocities, according to the following relations:

$$c_L = \sqrt{\frac{\lambda + 2\mu}{\rho}} \quad \text{and} \quad c_T = \sqrt{\frac{\mu}{\rho}} \tag{1}$$

* Corresponding author.
E-mail address: odile.abraham@lcpc.fr (O. Abraham).

0958-9465/$ - see front matter © 2006 Elsevier Ltd. All rights reserved.
doi:10.1016/j.cemconcomp.2006.02.014

where λ and μ are Lamé parameters (with μ being the shear modulus), ρ the density. Young's modulus is equal to

$$E = \frac{\mu(3\lambda + 2\mu)}{\lambda + \mu} \tag{2}$$

A comparison of wave speeds, measured along a tunnel for the same concrete, will thus enable zoning walls by degree of deterioration.

In the following discussion, longitudinal and surface waves will be combined, whenever possible, in order to determine longitudinal and transverse wave (L-wave and T-wave) velocities as a function of depth. When material properties increase with depth, which is the case herein, the c_L profile obtained with seismic refraction (SR) constitutes valuable a priori information for interpreting data from the multi-channel analysis of surface waves (MASW) [5,12]. It should be noted that concrete structures are viewed as 1-D media (in cases where material properties depend solely on distance from the surface). The limitations of this hypothesis have been discussed elsewhere [5].

Seismic refraction (SR) measurements and multi-channel analysis of surface waves (MASW) are classical geophysics tools [4,27] easily transferable to concrete NDE. They both rely upon the same experimental set-up, i.e. for a given shot point, a set of aligned and often equally spaced sensors. The data measured are the surface particle displacement (or velocity, or acceleration) amplitudes of each sensor as a function of time, hereafter called a "seismogram". Concrete SR surveys are limited to cases in which mechanical properties increase with depth (for instance, following fire damage [1]). SR techniques will yield the thickness of the damaged zone and its c_L value, along with the corresponding value for sound concrete.

MASW is gaining popularity within the field of civil engineering. For material characterization applications, the results produced consist of the thickness and c_T profile. MASW can be applied regardless of the variation in material properties with depth for: geotechnical purposes [17,11,8,2], road investigations [37,29], or underwater applications [34]. MASW has also been proposed for the localization and sizing of faults, e.g. cavities [19] or concrete crack depth [16,32].

The originality of this paper is to address the issue of concrete structure NDE with SR and MASW when the structure is not constituted of a superposition of flat layers, but instead is essentially axisymmetric, like in circular tunnels, and when the sensors are located on its circumference. It would seem that while the case of NDE of curved structures with sensors not localized inside the cylindrical cavity has been well-documented [3,35,14,10], such is no longer true when sensors lie inside a circular hole (i.e. concave surface). In this case, a spatial attenuation of surface waves appears due to energy radiation into the medium [36,9].

In the next section, we will illustrate the error introduced during SR interpretation of data recorded in a 1-D circular geometry should a 1-D plane model be used in its place. Our focus will then turn to surface waves; the basic physical principle behind surface wave investigation will be displayed before presentation of the equations governing the propagation of surface waves on concave surfaces. A subsequent section will be devoted to applying the physical phenomena and data interpretation to a reduced-scale physical concrete model. The numerical and experimental examples provided in this paper pertain to one-layer media (a layer, indexed 1, on top of an infinite medium, indexed 0), yet the physical phenomena discussed may be easily extended to multi-layered cases.

2. Seismic refraction

Whenever an incident wave encounters an interface, it is both reflected and refracted. Seismic refraction is based on Huygen's principle and makes use of refracted waves [33]. The underlying principle has been summarized in Fig. 1a for a one-plane layer of thickness e_1, with an L-wave speed equal to c_{L1}, on top of an infinite medium of L-wave speed c_{L0} (with $c_{L0} > c_{L1}$; seismic refraction is only valid when wave speed is increasing with depth). For an incident angle greater than the critical angle $i_c = \arcsin(\frac{c_{L1}}{c_{L0}})$, the refracted wave does not penetrate into the infinite medium but rather propagates along the interface. In order to determine the values of c_{L1}, e_1 and c_{L0}, the required information consists of the arrival time of the L-wave as a function of source-receiver distance, hereafter called offset (see Fig. 1b).

2.1. Within a plane medium

When the offset is less than a given crossover distance x_c (Eq. (3)), the first wave is the direct wave.

$$x_c = 2e_1\sqrt{\frac{c_{L0} + c_{L1}}{c_{L0} - c_{L1}}} \tag{3}$$

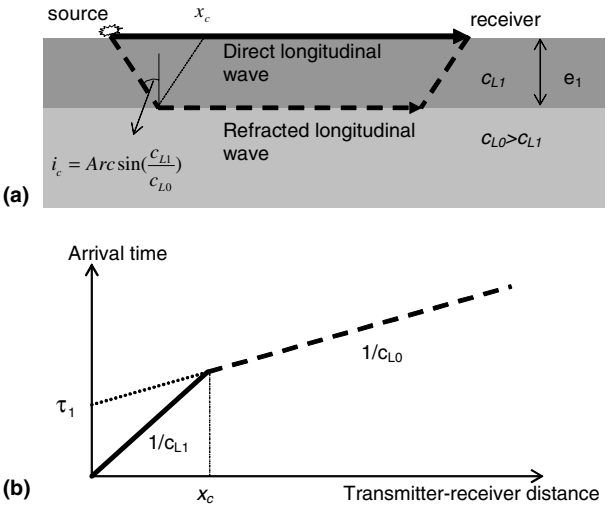

Fig. 1. Basic principle of seismic refraction illustrated for a one layer plane medium. (a) Ray path of the longitudinal wave for offsets greater than x_c. (b) Travel time as a function of the offset. The slope of each straight line gives the slowness of each layer. The thickness is computed using the intersection of the line of slope $\frac{1}{c_{L0}}$ with the y-axis.

The slope of the straight line before x_c can be used to determine c_{L1} (Fig. 1b) and the slope of the next straight line yields c_{L0}. The intersection of this line with the y-axis, τ_1, may then serve to calculate the thickness of the first layer

$$e_1 = \frac{c_{L1}\tau_1}{2\cos\left(\arctan\frac{c_{L1}}{c_{L0}}\right)} \quad (4)$$

This principle may be extended to several layers, as well as to dip layers, in which case several source points are required to recover the 2D geometry of the medium. This procedure is quite commonplace in the field of applied geophysics [33]. It will not be described herein since our data interpretation will be carried out using simple models based on 1-D (either plane or circular) concrete structures. We have shown in Fig. 2 an in situ example of the determination of damaged concrete thickness inside the Mont-Blanc Tunnel after the March 26, 1999 fire [1]. The measurements are located in a zone classified as heavily deteriorated by the "Autoroute du Tunnel du Mont-Blanc" authority. The L-wave velocity of damaged layer 1 actually equals $c_{L1} = 1130$ m/s, which is far less than the classical velocity of sound concrete (typically above 4000 m/s). Note that the L-wave velocity of the deeper medium ($c_{L0} = 3560$ m/s) is still below that of sound concrete: the damage extends to a depth beyond 0.09 m, i.e. the thickness e_1 of layer 1.

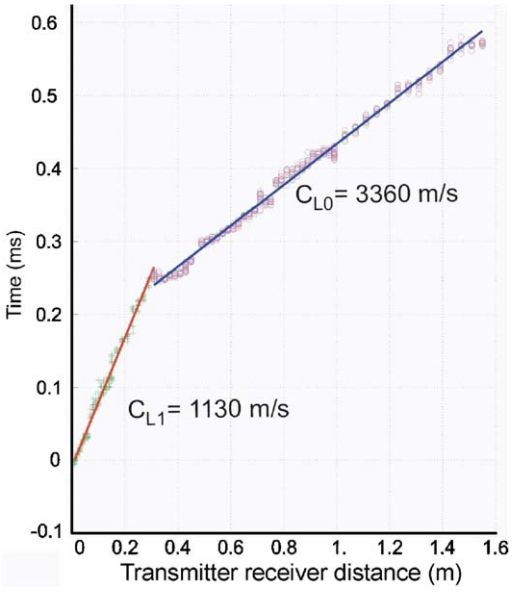

Fig. 2. Example of seismic refraction results of a concrete tunnel damaged by fire (Mont-Blanc Tunnel) interpreted with a 1D one-layer model.

2.2. Within a curved medium

In the case of circular concrete tunnels, the influence of curvature is not visible on the travel time–offset plots recorded along the circumference. A curved one-layer model ($R = 0.5$ m) with a damage zone thickness equal to $e_1 = 0.05$ m and an L-wave velocity $c_{L1} = 3360$ m/s on top of a medium with an L-wave velocity $c_{L0} = 3980$ m/s will yield, for example, the same travel time–offset plot as a plane one-layer model with a damage zone 0.062 m thick (and with the same longitudinal wave velocity) lying on top of a medium with an L-wave velocity equal to 3680 m/s instead of $c_{L0} = 3980$ m/s. In this case, if curvature were neglected, the thickness of the damaged zone would be overestimated (by 24%) and the L-wave velocity underestimated (by 9%).

Fig. 4 illustrates this result on the basis of a simple analytical model using optical geometry laws for both a plane model and a curved model with the same material properties ($c_{L1} = 3360$ m/s, $c_{L0} = 3980$ m/s) and thickness $e_1 = 0.05$ m. The direct L-waves, for the two models, follow the same line. The refracted L-waves feature different slope and crossover distance (x_c) values. For the plane model, the slope is equal to $\frac{1}{c_{L0}}$ and x_c is given in Eq. (3); for the curved model, the slope is equal to

$$\frac{R + e_1}{Rc_{L0}} \quad (5)$$

The crossover distance displays the following expression:

$$x_c = 2R\frac{\frac{c_{L0}}{c_{L1}}\sin\theta_c - \theta_c\frac{R+e_1}{R}\frac{c_{L1}}{c_{L0}}}{1 - \frac{R+e_1}{R}\frac{c_{L1}}{c_{L0}}} \text{ with } \theta_c \text{ solution of } \tan$$

$$i_c = \frac{R\sin\theta_c}{R(1-\cos\theta_c) + e_1} \text{ and the critical angle}$$

$$i_c = \arcsin\left(\frac{c_{L1}}{c_{L0}}\right) \quad (6)$$

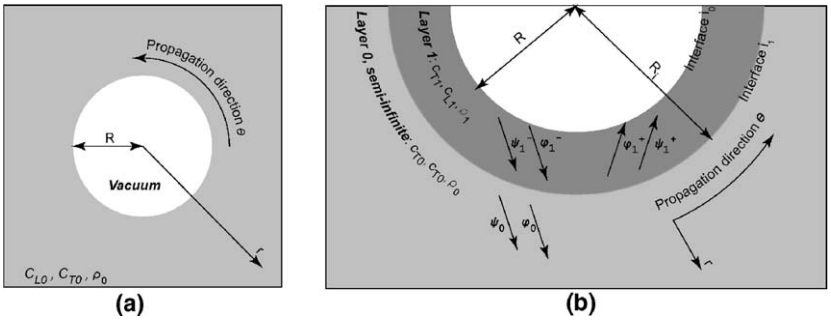

Fig. 3. Schematic view of the circular models and notations. (a) Homogeneous medium and (b) one-layer curved medium.

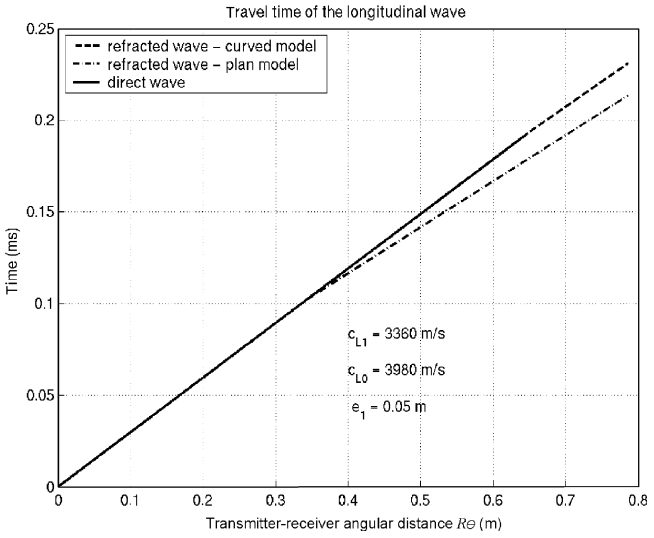

Fig. 4. Travel time of the longitudinal wave as a function of the offset for one-layer model with $e_1 = 0.05$ m, $c_{L1} = 3360$ m/s and $c_{L0} = 3980$ m/s either plane or curved (with $R = 0.5$ m). The plain line is the direct wave, the dashed line is the refracted wave of the curved model, the dashed-dotted line is the refracted wave of the plane model.

3. Surface waves within a 1-D plane medium

Surface waves (*R*-waves) offer the advantage of being sensitive to the shear modulus of concrete. In a homogeneous half-space, any seismic excitation on the surface generates a surface wave (called a Rayleigh wave) that propagates along a cylindrical wave front. At the surface, the displacement amplitude varies with $x^{-1/2}$ due to geometrical damping (where x is the offset), in comparison with x^{-1} for the *L*- and *T*-waves. *S*-waves are highly energetic since in the far-field, nearly 70% of the energy transmitted by a vertical point load source in an elastic isotropic and homogeneous half-space is propagated in this form [23]. Moreover, beyond a given depth, the particle displacement amplitude decreases exponentially. The investigation depth is thus related to wavelength [4] (the maximum energy of *R*-wave is approximately located at a depth of $\frac{\lambda}{3}$).

S-waves are derived from Navier's displacement equation of motion (7) as a sum of a scalar φ and a vector ψ displacement potentials (8) [13] related to longitudinal and transverse waves which coupled to the surface boundary and satisfy the stress-free surface boundary conditions

$$(\lambda+\mu)\nabla\nabla\cdot\mathbf{u}+\mu\nabla^2\mathbf{u}=\rho\frac{\partial^2\mathbf{u}}{\partial t^2} \tag{7}$$

$$\mathbf{u}=\nabla\varphi+\nabla\times\psi \tag{8}$$

λ and μ are the Lamé parameters and ρ is the density.

In the case of a medium characterized by c_{L0} and c_{T0}, and bounded by a plane free surface, the potentials of the propagating wave along the free boundary are of the following form:

$$Z(z)\mathrm{e}^{-\mathrm{i}k(x-c_R t)} \tag{9}$$

where c_R is the phase velocity of the *R*-waves and k is the wavenumber.

3.1. Homogeneous half-space

In a homogenous half-space, c_R is calculated from the Rayleigh equation (Eq. (10)) [28]

$$4\left(1-\frac{c_R^2}{c_{L0}^2}\right)^{\frac{1}{2}}\left(1-\frac{c_R^2}{c_{T0}^2}\right)^{\frac{1}{2}}=\left(2-\frac{c_R^2}{c_{T0}^2}\right)^2 \tag{10}$$

An approximation of c_R yields:

$$c_R=\frac{1.12\nu+0.87}{1+\nu}c_{T0} \tag{11}$$

where ν corresponds to the Poisson's ratio.

As presented in Eq. (11), c_R is related to the transverse wave velocity (for Poisson's ratios of between 0 and 0.5, c_R varies from 0.87 c_{T0} to 0.96 c_{T0}). *R*-waves thus provide a valuable means for recovering the *T*-wave velocity, which is directly linked to the shear modulus via Eq. (1). This surface wave is called the Rayleigh wave [28].

3.2. Multi-layered half-space

One particularity of *R*-waves is to be dispersive within a multi-layered medium: c_R becomes a function of frequency. For a given frequency content of the seismic source, low-frequency *R*-waves will travel deeper than high-frequency waves. If material properties vary with depth, the dispersion curve (phase and/or group velocities of *R*-waves) will carry information on the *L*-wave velocity (and on *T*-wave velocity and ρ, albeit with less sensitivity) of the shallower layers at higher frequency and of the deeper layers at lower frequency. A second particularity of *S*-waves within a

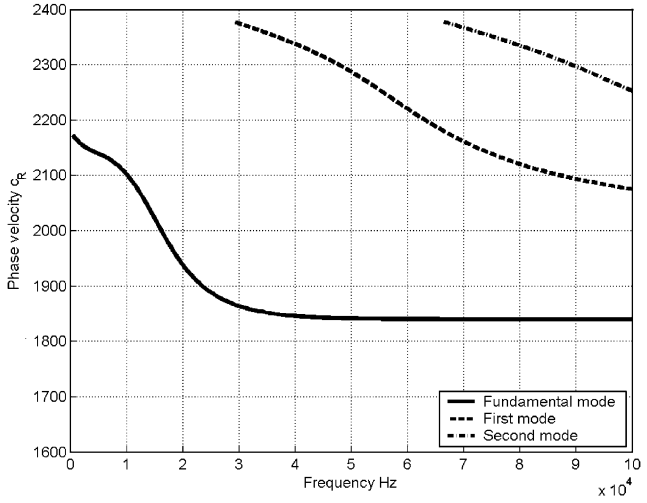

Fig. 5. Phase velocity dispersion curves of the first three modes of the surface waves for a one-layer model. Layer: $e_1 = 0.05$ m, $c_{L1} = 3360$ m/s, $c_{T1} = 2012$ m/s, $\rho_1 = 1900$ kg m^{-3} Infinite medium: $c_{L0} = 3980$ m/s $c_{T0} = 2384$ m/s, $\rho_0 = 2400$ kg m^{-3}.

multi-layered half-space is their multi-modal propagation. Different modes of propagation may exist for the same frequency with varying propagation depths and velocities [4].

Fig. 5 shows the phase velocity dispersion curves of the first three modes for the one-layer model studied in the section on SR above. It can be seen that over the high-frequency range, the fundamental mode converges towards the *R*-wave velocity of the shallow layer, whereas over the low-frequency range it converges towards the *R*-wave velocity of the semi-infinite medium.

The current processing technique consists of recording a seismogram, then determining the experimental phase velocity dispersion curves, and lastly inversing the dispersion curve in order to recover the *T*-wave profile by matching the experimental dispersion curve with a numerical curve. The main drawbacks of the MASW technique are: the non-uniqueness of the inverse problem solution inherent in most inverse problems; multi-modal propagation that may lead to measuring what is called an effective phase velocity dispersion curve [11,26]; the limitations inherent in the 1-D assumption [5,15]; and an investigation depth that may not match requirements [5,25]. These drawbacks would also be valid for *R*-waves in curved media; they will not be addressed in the following section given that our models, whether numerical or experimental, are truly 1-D and designed to correlate with our experimental equipment. The second and higher modes are well-separated from the fundamental mode, which will be the only one considered hereafter.

4. Surface waves for a curved medium

4.1. Homogeneous medium

As opposed to Rayleigh wave propagation within a homogeneous half-space medium bounded by a plane-free surface, the propagation of surface waves along a circular surface encounters dispersion and features a phase velocity less than that of the Rayleigh wave [36]. The aim of this section is to quantify the influence of this dispersion on the basis of model simulations.

4.1.1. Analytic determination of the characteristic function

After rewriting Navier's displacement Eq. (7) of motion in cylindrical coordinates (r,θ) (see Fig. 3) and using Helmholtz's theorem (Eq. (8)), the decoupled propagation equations governing the axisymmetric scalar φ and vector ψ displacement potentials (Eq. (9)) within a linear, elastic isotropic medium with invariance along the r direction can then be obtained

$$\begin{cases} \rho\frac{\partial^2\varphi(r,\theta,t)}{\partial t^2} = (\lambda+2\mu)\left(\frac{\partial^2}{\partial r^2}+\frac{1}{r}\frac{\partial}{\partial r}+\frac{1}{r^2}\frac{\partial^2}{\partial\theta^2}\right)\varphi(r,\theta,t) \\ \rho\frac{\partial^2\psi(r,\theta,t)}{\partial t^2} = \mu\left(\frac{\partial^2}{\partial r^2}+\frac{\partial}{\partial r}\frac{1}{r}+\frac{\partial^2}{\partial\theta^2}\right)\psi(r,\theta,t) \end{cases} \quad (12)$$

The potentials for propagation along the concave surface of a circular cavity are, according to Viktorov [36], of the following form:

$$\varphi = \varphi_0 H_n^{(1)}(k_L r)e^{i(n\theta-\omega t)} \quad (13)$$

$$\psi = \psi_0 H_n^{(1)}(k_T r)e^{i(n\theta-\omega t)} \quad (14)$$

where $H_n^{(1)}$ is the Hankel function of the first kind of order n (i.e. it represents a cylindrical divergent wave in accordance with the chosen time dependence), $\omega = 2\pi f$ is the pulsation with f the frequency, $k_L = \omega/c_{L0}$ and $k_T = \omega/c_{T0}$ are the *L*- and *T*-wave radial wave numbers, respectively. $n = \omega R/c_R$ is the orthoradial wave number, $k_\theta = \omega/c_R$, normalized with respect to cavity radius R (with c_R being the surface wave phase velocity).

The Hankel functions have been chosen to satisfy the vanishing radiation at infinity.

Cancellation of the tangential $\sigma_{r\theta}$ and normal σ_{rr} stresses at the free surface leads to the following characteristic function [9], equivalent to Eq. (10) for the curved medium

$$(\beta^2-2)^2 - 4 - \left(\frac{4\beta^2}{n}\right) + H_\beta\left[4+\left(\frac{2\beta^2}{n}\right)-\left(\frac{2}{n}\right)^2\right] + H_\alpha\left[4+\left(\frac{2\beta^2}{n}\right)-\left(\frac{2}{n}\right)^2 - H_\beta\left(4-\left(\frac{2}{n}\right)^2\right)\right] = 0 \quad (15)$$

with

$$\beta = c_R/c_{T0} \quad \text{and} \quad \alpha = c_R/c_{L0}$$

$$H_\alpha = \frac{\alpha H_{n-1}^{(1)}(k_L R)}{H_n^{(1)}(k_L R)} \quad \text{and} \quad H_\beta = \frac{\beta H_{n-1}^{(1)}(k_T R)}{H_n^{(1)}(k_T R)}$$

At this stage, it is worth noting that n is a complex quantity (as is the related orthoradial wave number $k_\theta = k_1 + jk_2$). A surface wave thus propagates along a concave surface with attenuation. This leakage in the surrounding medium is due to radial radiation; such a wave will hereafter be called the leaky circumferential surface wave (i.e. the LCS-wave).

The dispersion relations, derived from the wave number and frequency solutions to the characteristic equation in the form of phase velocity versus frequency for the plane-surface Rayleigh wave case (Eq. (10)), must include a third solution parameter relative to wave attenuation for the LCS-wave case.

As opposed to the majority of situations found in the literature [36,9], wherein high-frequency or large-radius conditions (typically $n > 100$) lead to a negligible k_2 contribution and hence to great simplification of the characteristic Eq. (15) resolution, our study configuration (typically $2 < n < 70$) implies giving consideration to the attenuation-related term k_2. The dispersion curves are therefore derived by numerical searches for the (k_1, k_2, f) triplets that satisfy the characteristic Eq. (15). Complex-order Hankel functions are calculated using the NSWC (Naval Surface Warefare Center) FORTRAN library. The different numerical libraries that compute these kinds of functions are described in [21,22].

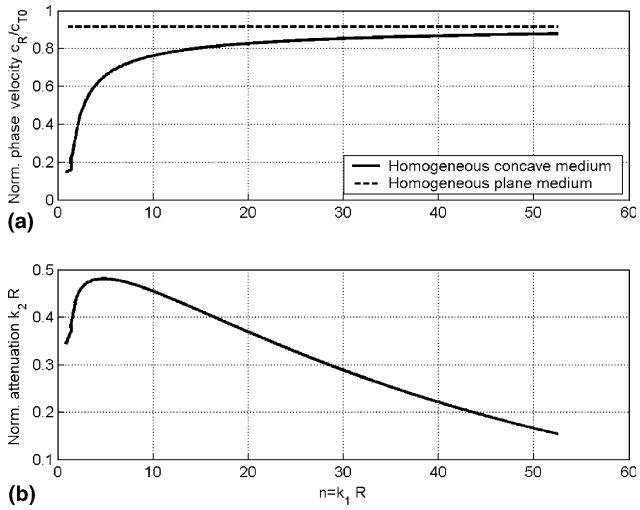

Fig. 6. Normalized phase velocity (a) and attenuation (b) dispersion curves for a concave homogenous media ($v_0 = 0.22$ and $\rho_0 = 2400$ kg m^{-3}, radius of the cavity $R = 0.5$ m and n is the angular wave number).

4.1.2. Numerical results

Fig. 6a displays normalized numerical dispersion curves, obtained using the characteristic function (15), where the phase velocity c_R has been normalized with respect to c_{T0} and plotted with respect to n. The parameters included in this model are: $c_{T0} = 2384$ m/s, $c_{L0} = 3980$ m/s (Poisson's ratio $v = 0.22$), density $\rho_0 = 2400$ kg m^{-3}, and cylinder radius $R = 0.55$ m. The dotted curve represents the normalized Rayleigh wave phase velocity (plane medium), while the solid curve corresponds to the normalized LCS-wave phase velocity calculated for a concave medium. This figure also shows that the LCS-wave phase velocity decreases as n tends towards zero; this velocity tends towards the Rayleigh wave phase velocity as n increases. When frequency is low (i.e. small n), the wavelength is large; hence the distance traveled by the LCS-wave clearly becomes larger and involves lower-phase velocities, whereas as frequency rises (large n), the wavelength is small and the curvature effect becomes negligible.

Fig. 6b displays the numerical attenuation dispersion curve, in which the imaginary part, k_2, or the LCS-wave wave number is normalized with respect to R and then plotted with respect to n. This figure also indicates that k_2 reaches its maximum at low frequencies (small n) and then monotonically decreases towards zero with increasing frequency.

4.2. Multi-layered half-space

The characteristic function, described in the previous section and which enables computing theoretical dispersion curves, is much more difficult to obtain in the case of a multi-layered half-space. The easiest approach to determining the characteristic function in the presence of a multilayer is to use the global matrix method.

The global matrix method, proposed by Knopoff [18] and implemented as described by Lowe [20], consists in sum of assembling into a system matrix $\mathbf{S}$ a set of layer-interface matrices $\mathbf{D}_{li}$ that serve to describe the displacement-stress field associated with harmonic wave propagation at an interface i into a layer l. The theoretical dispersion curves are thus generated by means of numerical searches for the (k_1, k_2, f) triplets that solve the characteristic function, which in this case assumes the following form:

$$f(k_1, k_2, f) = \det[\mathbf{S}] = 0 \tag{16}$$

The global matrix formulation will be explained in greater detail in the next Section 4.3 for the one-layer case.

4.3. One-layer case

4.3.1. Global matrix formulation

In order to obtain the characteristic function for an elastic annulus embedded within an infinite elastic medium, the layer-interface matrix $\mathbf{D}$ at each interface of the model must first be determined analytically. In the one-layer model considered hereafter, two layers and two interfaces are involved and they result in three layer-interface matrices $\mathbf{D}$ to be determined.

To begin, in following an approach similar to that described in Section 4.1 on the homogeneous case, the decoupled propagation equations governing the axisymmetric scalar and vector displacement potentials in a linear, elastic isotropic and homogeneous discrete layer, with invariance along the r direction, will be formulated.

The expressions for the solution to potentials for propagation inside discrete layer 1 are of the following form:

$$\varphi = (\varphi_1^+ H_n^{(2)}(k_L r) + \varphi_1^- H_n^{(1)}(k_L r))\mathrm{e}^{\mathrm{i}(n\theta - \omega t)} \tag{17}$$

$$\psi = (\psi_1^+ H_n^{(2)}(k_T r) + \psi_1^- H_n^{(1)}(k_T r))\mathrm{e}^{\mathrm{i}(n\theta - \omega t)} \tag{18}$$

where $H_n^{(2)}$ and $H_n^{(1)}$ are Hankel function of the second kind representing a cylindrically convergent partial wave in a bounded medium, and of the first kind, representing a cylindrically divergent partial wave in a bounded medium, respectively. The terms $\varphi_1^+, \varphi_1^-, \psi_1^+$ and ψ_1^- represent the amplitudes of the partial waves [30] described on Fig. 3 and are related to the longitudinal convergent and divergent, and the transverse convergent and divergent, respectively (see Fig. 3).

From Helmholtz's theorem, the normal and radial displacements are obtained first and then the tangential and normal stresses are classically derived from such displacements using Hooke's Law. The displacement and stress fields inside the shallow layer $l1$ at each interface can thus be expressed in the following matrix form:

$$\begin{bmatrix} u_r \\ u_\theta \\ \sigma_{rr} \\ \sigma_{r\theta} \end{bmatrix}_{i_1} = [\mathbf{D}_{i_1 l_1}] \begin{bmatrix} \varphi_1^+ \\ \varphi_1^- \\ \psi_1^+ \\ \psi_1^- \end{bmatrix} \text{ at the layer/semi-infinite medium interface } i_1 \text{ and}$$

$$\begin{bmatrix} \sigma_{rr} \\ \sigma_{r\theta} \end{bmatrix}_{i_0} = [\mathbf{D}_{i_0 l_1}] \begin{bmatrix} \varphi_1^+ \\ \varphi_1^- \\ \psi_1^+ \\ \psi_1^- \end{bmatrix} = 0 \text{ at the free surface } i_0 \tag{19}$$

Using a similar approach, along with the results obtained in Section 4.1, the layer-interface matrix D_{i1l0} at interface i_1 in the semi-infinite medium l_0 is determined

$$\begin{bmatrix} u_r \\ u_\theta \\ \sigma_{rr} \\ \sigma_{r\theta} \end{bmatrix}_{i_1} = [\mathbf{D}_{i_1 l_0}] \begin{bmatrix} \varphi_0 \\ \psi_0 \end{bmatrix} \tag{20}$$

Once the three-layer interface matrices **D** have been calculated for each interface in shallow layer l_1 and in semi-infinite medium l_0, the global matrix **S** can be assembled by fulfilling the boundary conditions, which are null: stresses at the free surface i_0 and stress-displacement continuity through i_1.

$$\begin{bmatrix} \sigma_{rr}^{i_0 l_1} \\ \sigma_{r\theta}^{i_0 l_1} \\ u_r^{i_1 l_1} - u_r^{i_1 l_0} \\ u_\theta^{i_1 l_1} - u_\theta^{i_1 l_0} \\ \sigma_{rr}^{i_1 l_1} - \sigma_{rr}^{i_1 l_0} \\ \sigma_{r\theta}^{i_1 l_1} - \sigma_{r\theta}^{i_1 l_0} \end{bmatrix} = [\mathbf{S}] \begin{bmatrix} \varphi_1^+ \\ \varphi_1^- \\ \psi_1^+ \\ \psi_1^- \\ \varphi_0 \\ \psi_0 \end{bmatrix} = 0 \quad \text{where } \mathbf{S} = \begin{bmatrix} \mathbf{D}_{i_0 l_1} & [\mathbf{0}] \\ \mathbf{D}_{i_1 l_1} & -\mathbf{D}_{i_1 l_0} \end{bmatrix} \tag{21}$$

The matrix **S** is shown in Appendix A.

In this particular case, $\mathbf{D}_{i0l1}$ is a four-by-two matrix given that it incorporates the free-surface boundary condition, $\mathbf{D}_{i1l1}$ is a four-by-four matrix and $\mathbf{D}_{i1l0}$ is a two-by-four matrix given the absence of incoming waves in the semi-infinite medium. The resultant **S** is a six-by-six matrix.

4.3.2. Numerical results

Fig. 7a displays the normalized numerical dispersion curve for the fundamental mode, as obtained with the global matrix method (Eqs. (16) and (21)), wherein phase velocity c_R has been normalized with respect to the *T*-wave velocity of layer 1 c_{T1} and plotted with respect to n. The parameters used for this model are: $c_{T0} = 2384$ m/s, $c_{L0} = 3980$ m/s (Poisson's ratio $v = 0.22$), density $\rho_0 = 2400$ kg m^3 for the elastic semi-infinite medium, $c_{T1} = 2012$ m/s, $c_{L1} = 3360$ m/s (Poisson's ratio $v = 0.22$), and density $\rho_1 = 1900$ kg m^3 for the elastic annulus. The cavity radius $R = 0.5$ m and the elastic annulus thickness e is equal to 0.05 m. At low n, the one-layer medium normalized phase velocity c_R (solid curve in Fig. 7a) increases, following the same trend as that of a semi-infinite curved medium with c_{T1}, c_{L1}, ρ_1 characteristics and radius R (dotted-dashed curve) and reaches a maximum for $n = 22$–23. At high n, c_R converges towards the normalized phase velocity of a semi-infinite curved medium with c_{T0}, c_{L0}, ρ_0, characteristics (dashed curve).

In other terms, when frequency is low (small value of n), the wavelength is obviously large and the major part of the Rayleigh LCS-wave energy is propagating in the semi-infinite medium without being influenced by the elastic annulus. On the other hand, when frequency rises (large n), the wavelength is small and the major part of the LCS-wave energy is propagating inside the elastic annulus, with the effect of the semi-infinite medium becoming negligible.

Fig. 7b depicts the numerical dispersion curve, where the attenuation term k_2 has been normalized with respect to cavity radius R and plotted with respect to the LCS-wave orthoradial, normalized wave number n. This figure shows that k_2 reaches its maximum at a lower frequency ($n = 5$) and then decreases towards zero at increasing frequencies. It is important to point out that this decrease is much more prominent than for the concave homogeneous model, due to trapping the leaky LCS-wave within the elastic layer subsequent to multiple reflections at its boundaries [3].

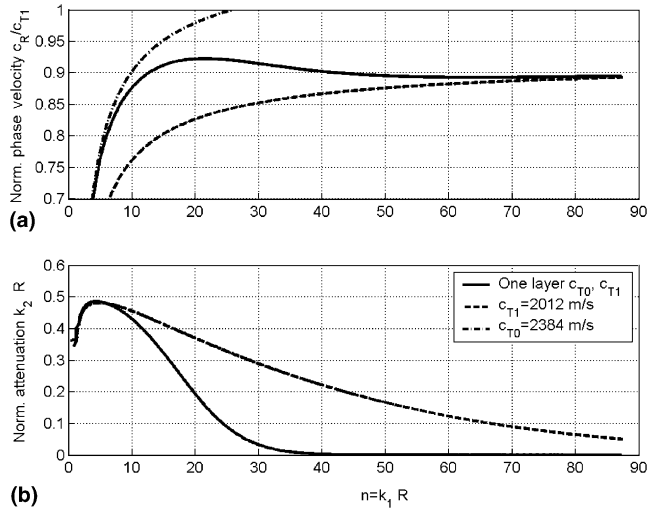

Fig. 7. Normalized phase velocity (a) and attenuation (b) dispersion curves (fundamental mode) for a concave one-layer media ($v_0 = v_1 = 0.22$, $\rho_0 = \rho_1 = 2400$ kg m^{-3}, thickness $e_1 = 0.05$ m, radius of the cavity $R = 0.5$ m and n is the angular wave number).

5. Experiments conducted on curved media

5.1. Reduced-scale physical model and experimental set-up

The objective of a reduced-scale physical model is to obtain data for a perfectly known model. In this case, the purpose entails recording experimental data in order to observe an experimental phase velocity dispersion curve and then compare this curve with numerical data.

The development of such a model requires precise proportions representative of a real case. Moreover, its scale must remain large enough in order to avoid border effects. (Surface wave reflections on borders can disturb data.)

Fig. 8a and b exhibit a schematic top view (a) and side view (b) representing the proportions of the derived reduced-scale physical model; it consists of a block 5.1 m × 3.1 m × 2.1 m and two holes 2.1 m high with an inside radius equal to 0.55 m. A bold black curve shows the location of sensors around the cylindrical cavity.

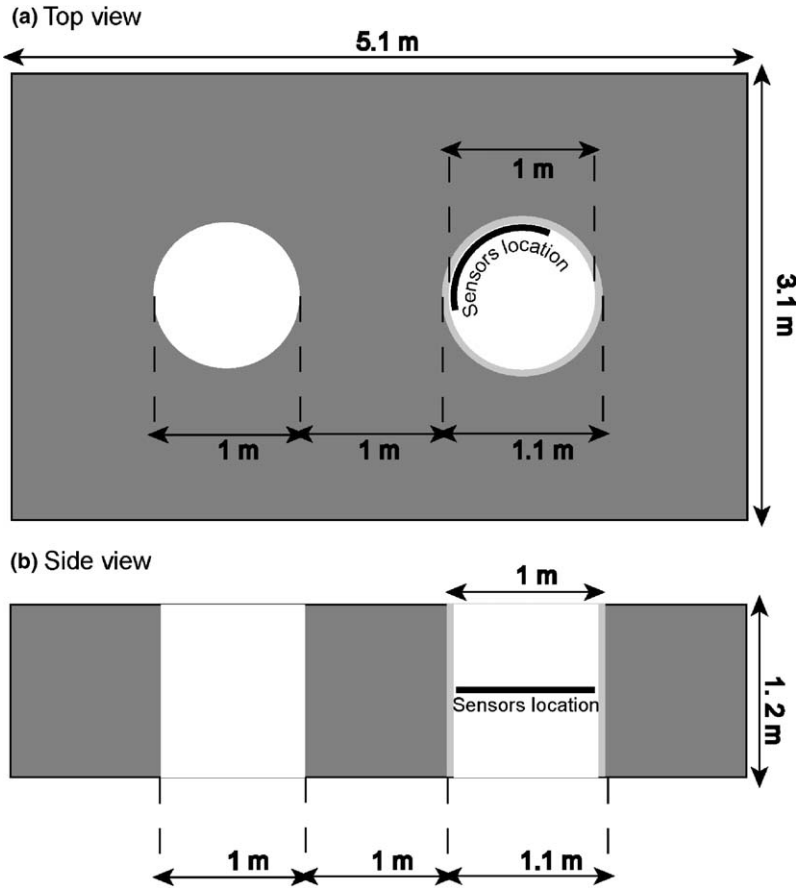

Fig. 8. Schematic representation and dimension of the concrete reduced scale physical model. The dark grey indicates concrete and the light grey mortar. The thick line shows the location of the accelerometers. (a) Top view and (b) side view.

The various materials used to build this model, as indicated by differing shades of grey on the figure, are as follows. The dark gray area corresponds to the concrete, specially designed to avoid grain segregation and strengthened with plastic fibers in order to limit cracking and obtain a medium as homogeneous as possible. The clear gray area corresponds to a mix of lime and mortar with an adhesive additive to ensure good contact between the two materials with thickness $e_1 = 0.05$ m. L-wave velocity measurements on both materials have been performed and yield $c_{L1} \approx 3360$ m/s for the mortar and $c_{L0} \approx 3980$ m/s for the concrete.

An initial step of surface waves and seismic refraction measurements in both cylindrical cavities was conducted before the mortar layer was installed. The layout was composed of 23 accelerometers, spaced every 5 cm and located around the circumference of each cavity, for a total length of 1.1 m between the first and last sensors. The accelerometers used were Brüel & Kjaer No. 4393, with a frequency range from 0.1 to 16.5 kHz and a sensitivity of 3.1 pC g^{-1}. Various types of sources were tested at different offsets from the sensors (hammer, metallic balls), with a global frequency band lying between 5 and 20 kHz.

A second surface wave and seismic refraction series of experiment, using the same layout and sources, was then performed after installation of the mortar layer.

5.2. Measured seismograms

Fig. 9a and b present typical recordings from a receiver spread located along the circumference of the cylindrical cavity, as indicated in Fig. 8. These seismograms have been obtained both before (Fig. 9a) and after (Fig. 9b) installing the mortar layer.

The seismic source here is a hammer shock. The hammer used has a mass of 100 g. The transient acquisition system has 32 channels with a measured resolution of 12 bits. The acquisition is triggered by one accelerometer located one centimeter away from the impact point. The sampling frequency is equal to 1 MHz. Each of the 23 traces recorded consists of 4096 samples.

Three kinds of waves may be observed on these figures and have been drawn in Fig. 9a and b:

- LCS-wave, processed by means of computing its phase velocity dispersion curve through use of the p–ω method described in the following section;
- L-waves, whose first arrivals are captured and processed by the seismic refraction method; and
- LCS-wave reflections on the borders of the physical model and the LCS-wave propagating in the opposite direction along the circumference. All these waves are

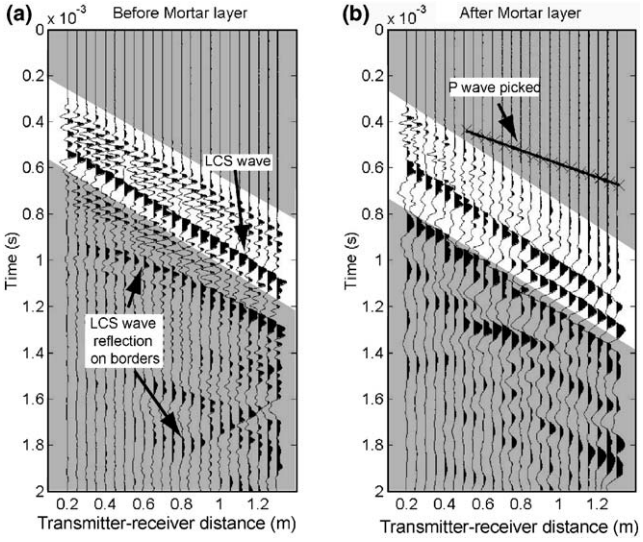

Fig. 9. Normalized seismogram recorded along the circumference of the holes. The white zones correspond to the signal effectively used for the computation of the dispersion diagram. (a) Before installing mortar layer ($R = 0.55$ m). (b) After installing the mortar layer ($e_1 = 0.05$ m and $R = 0.5$ m). The thick line indicated the time of arrival of the refracted L-wave.

considered as noise and hence must be windowed. The white area on both seismograms depicts the limits of the window applied on each trace.

5.3. Determination of the experimental dispersion curve

In the following discussion, the experimental phase velocity dispersion curves will be calculated using the p–ω technique proposed by [24] and based on the work of [31]. According to this setup, p stands for the slowness, i.e. the inverse of phase velocity, and ω is the angular frequency. The signal recorded at distance x_n from the source can be written in the frequency domain as:

$$s(\omega, x_n) = A(\omega, x_n)\mathrm{e}^{\mathrm{i}\phi_n(\omega)} \tag{22}$$

where $A(\omega, x_n)$ and $\phi_n(\omega)$ are the amplitude and phase of the signal spectrum, respectively.

The p–ω transform consists, after correction of the geometric attenuation for each signal, of calculating the following summation:

$$F(\omega, p) = \sum_{n=1}^{\text{total number of traces}} \frac{A(\omega, x_n)\mathrm{e}^{\mathrm{i}(\phi_n(\omega)+\omega p x_n)}}{A(\omega, x_1)\mathrm{e}^{\mathrm{i}\phi_1(\omega)}} \tag{23}$$

In the far-field, typically when the signal can be considered as a summation of plane waves, a maximum of function F within the p–ω plane is indicative of a phenomenon that travels with phase velocity $1/p$ at angular frequency ω.

Whenever possible, it is recommended to first determine the p–ω transform for a long spread (typically twice the larger expected wavelength) and then to remove the near-field traces [5].

In the reduced-scale model, the larger wavelength calculated from the lower frequency on the frequency band used is near 0.4 m. The seismograms employed (Fig. 9a and b) start with offsets equal to 0.2 m and are 1.1 m long.

5.4. Surface wave results

5.4.1. Homogeneous media

Fig. 10 exhibits the experimental dispersion diagram of the seismogram represented in Fig. 9a, as computed using

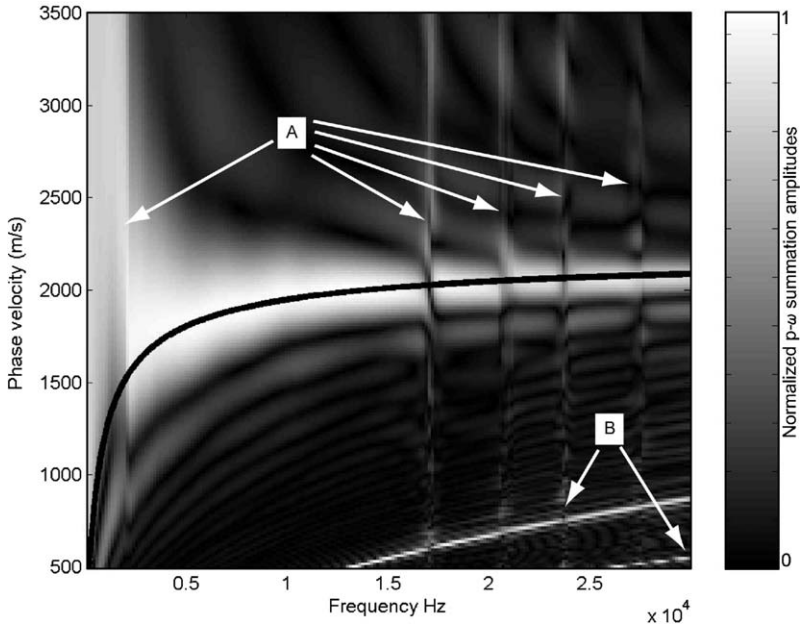

Fig. 10. Experimental dispersion diagram obtained from the seismogram represented Fig. 9a of the homogeneous concrete medium. The grey scale corresponds to p–ω normalized amplitudes. The numerical phase velocity dispersion curve (black curve) has been computed using reduced scale model a priori information. The arrows A correspond to discontinuities due to a lack of energy in the frequency domain and the B arrows characterizes spatial aliasing.

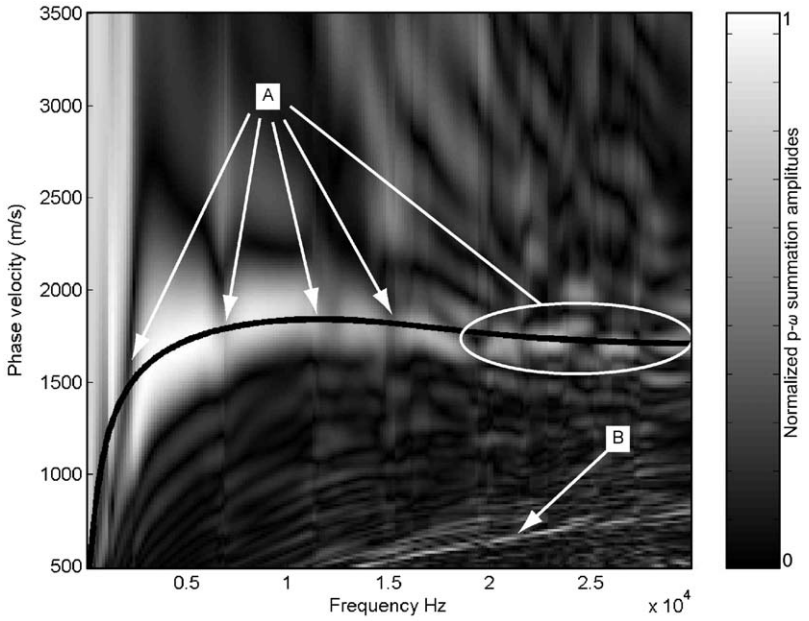

Fig. 11. Experimental dispersion diagram obtained from the seismogram represented Fig. 9b of the one-layer medium. The grey scale corresponds to p–ω normalized amplitudes. The numerical phase velocity dispersion curve (black curve) has been computed using reduced scale model a priori information. The arrows A and the with circled zone correspond to discontinuities due to a lack of energy in the frequency domain and the B arrow characterizes spatial aliasing.

the p–ω method described above. The experimental phase velocity of the fundamental mode of the LCS-wave is obtained by selecting the maximum normalized amplitudes from the diagram at each frequency point. In this case, this experimental phase velocity is located in the white area appearing between 1500 m/s and 2250 m/s. Some common artifacts also appear on this diagram. First of all, five discontinuities (indicated by the letter A on Fig. 10) coincide with a lack of energy over the frequency domain and with interfering waves such as the L-wave, plus second straight white lines (indicated by the letter B on Fig. 10) due to spatial aliasing (which does not deteriorate the phase velocity dispersion curve).

The black curve added on top of the p–ω transform corresponds to the numerical dispersion curve obtained with the global matrix method described in Section 4.1. The parameters used for computing this curve are based on the reduced-scale model's cavity radius dimension $R = 0.55$ m as well as on L-wave velocity measurements obtained by picking the first arrivals ($c_{L0} = 3980$ m/s). In this case, the numerical dispersion curve is clearly located in the p–ω maximum amplitude (white) area and thus closely fits the experimental data for a value of $c_{T0} = 2384$ m/s, which corresponds to a Poisson's ratio of 0.22. Measurements of both the LCS-wave phase velocity with the p–ω transform and the L-wave velocity, in combination with the model presented in Section 4.1, make it possible to estimate the Poisson's ratio of the concrete.

5.4.2. The one-layer case

In applying a similar approach, Fig. 11 displays both the experimental dispersion diagram generated from the seismogram shown in Fig. 9b and the numerical dispersion curve calculated with the global matrix method. The parameters used for the computation are: the values of c_{T0} and c_{L0} measured before installing the mortar layer (Section 5.4.1), the values of c_{L1} measured on cores, and a value of $c_{T1} = 2012$ m/s. The numerical dispersion curve obtained using the characteristic function (Eqs. (16) and (21)) is located in the p–ω transform maximum amplitudes (white zone) area and therefore correctly fits the experimental data and thus verifies this numerical model. It should be noted that the slope of the line indicating the first arrival of the L-wave (see Fig. 9b) for the furthest sensors yields a velocity equal to 3450 m/s, which is consistent with Eq. (5) and the actual value of c_{L0}.

6. Conclusion

Longitudinal and surface wave propagation in homogeneous and one-layer concave cylindrical structures has been investigated herein both numerically and experimentally. Numerical results for the surface wave rely upon an algorithm based on the global matrix method previously developed for multi-layered plane media. The generalization of this algorithm to all concave structures has led to significant numerical developments, due to the complex nature of surface wave phase velocity. Numerical results indicate an influence from curvature, in comparison with a plane medium, along with a non-negligible impact on the estimation of longitudinal wave velocity using the current seismic refraction method as well as on surface wave phase velocity values. The results presented in fact show that if this effect is neglected, longitudinal wave velocity may be underesti-

mated and the damaged layer thickness overestimated. The surface wave phase velocity is significantly underestimated at low frequencies in the case of multiple-channel analysis of surface wave (MASW) measurements. Furthermore, the surface wave propagates along the circumference of concave structures, with attenuation due to the radial radiation of energy into the medium. This geometrical attenuation exerts an impact on phase velocity values at low frequencies.

The numerical estimations are in good agreement with measurements taken on a reduced-scale concrete model, which experimentally confirms the curvature effect. The next step in our research work is to develop a robust inversion procedure for MASW phase velocity dispersion curves based on the direct model presented. The objective therein is to recover the *T*-wave velocity profile of multi-layered concave media. This inverse algorithm will be tested on the reduced-scale model as well as on in situ data recorded in tunnels or galleries.

The experimental example described on a reduced-scale concrete model has shown that seismic refraction and MASW are indeed complementary methods. Seismic refraction results should be employed whenever possible as a priori information for the MASW inverse problem procedure. It should be noted that even if velocity is not increasing with depth (a compulsory condition for the seismic refraction survey), the MASW method will still be applicable. This configuration is obtained, for instance, when the objective of the non-destructive testing survey consists of characterizing a material behind a concrete wall.

Acknowledgements

The authors would like to thank the INPL, ANDRA and INERIS organizations for supporting our research. Sincere gratitude is also addressed to Mr. Jacques Alexandre and the entire LCPC technical staff for their assistance in designing and building the reduced-scale physical model.

Appendix A

$$S=\begin{bmatrix}
\left[(2+2/n-\beta^2)J_{\alpha 1a0}-2\alpha/nJ_{\alpha 1a}\right] & 2(\beta J_{\beta 1a}-(1+1/n)J_{\beta 1a}) & \left[(2+2/n-\beta^2)Y_{\alpha 1a0}-2\alpha/nY_{\alpha 1a}\right] & 2(\beta Y_{\beta 1a}-(1+1/n)Y_{\beta 1a}) & 0 & 0\\
2(\alpha J_{\alpha 1a}-(1+1/n)J_{\alpha 1a}) & \left[(2+2/n-\beta^2)J_{\beta 10}-2\beta/nJ_{\beta 1a}\right] & 2(\alpha Y_{\alpha 1a}-(1+1/n)Y_{\alpha 1a}) & \left[(2+2/n-\beta^2)Y_{\beta 1a0}-2\beta/nY_{\beta 1a}\right] & 0 & 0\\
\alpha g J_{\alpha 1}-1 & 1 & \alpha g Y_{\alpha 1}-1 & 1 & \alpha_0 g H_\alpha-1 & 1\\
1 & \beta g J_{\beta 1}-1 & 1 & \beta g Y_{\beta 1}-1 & 1 & \beta_0 g H_\beta-1\\
\gamma(2-\beta^2g^2-2/n(\alpha g J_{\alpha 1}-1)) & 2(\gamma\beta g J_{\beta 1}-1/n-1) & \gamma(2-\beta^2g^2-2/n(\alpha g Y_{\alpha 1}-1)) & 2(\gamma\beta g Y_{\beta 1}-1/n-1) & 2-\beta^2g^2-2/n(\alpha_0 g H_\alpha-1) & 2(\beta_0 g H_\beta-1/n-1)\\
2(\gamma\alpha g J_{\alpha 1}-1/n-1) & \gamma(2-\beta^2g^2-2/n(\beta g J_{\beta 1}-1)) & 2(\gamma\alpha g Y_{\alpha 1}-1/n-1) & \gamma(2-\beta^2g^2-2/n(\beta g Y_{\beta 1}-1)) & 2(\alpha_0 g H_\alpha-1/n-1) & 2-\beta^2g^2-2/n(\beta_0 g H_\beta-1)
\end{bmatrix}$$

with

$$\alpha=\frac{c_R}{c_{L1}},\quad \alpha_0=\frac{c_R}{c_{L0}},\quad \beta=\frac{c_R}{c_{T1}},\quad \beta_0=\frac{c_R}{c_{T0}},\quad \gamma=\frac{\mu_1}{\mu_0},\quad g=\frac{Ri}{R},\quad H_\alpha=\frac{H_{n-1}(k_LRi)}{H_n(k_LRi)},\quad H_\beta=\frac{H_{n-1}(k_TRi)}{H_n(k_TRi)},$$
$$J_{\alpha 1}=\frac{J_{n-1}(k_LRi)}{J_n(k_LRi)},\quad J_{\beta 1}=\frac{J_{n-1}(k_TRi)}{J_n(k_TRi)},\quad Y_{\alpha 1}=\frac{Y_{n-1}(k_LRi)}{Y_n(k_LRi)},\quad Y_{\beta 1}=\frac{Y_{n-1}(k_TRi)}{Y_n(k_TRi)},\quad J_{\alpha 1a}=\frac{J_{n-1}(k_LR)}{J_n(k_LRi)},\quad J_{\beta 1a}=\frac{J_{n-1}(k_TR)}{J_n(k_TRi)},$$
$$Y_{\alpha 1a}=\frac{Y_{n-1}(k_LR)}{Y_n(k_LRi)},\quad Y_{\beta 1a}=\frac{Y_{n-1}(k_TR)}{Y_n(k_TRi)},\quad J_{\alpha 1a0}=\frac{J_n(k_LR)}{J_n(k_LRi)},\quad J_{\beta 1a0}=\frac{J_n(k_TR)}{J_n(k_TRi)},\quad Y_{\alpha 1a0}=\frac{Y_n(k_LR)}{Y_n(k_LRi)},\quad Y_{\beta 1a0}=\frac{Y_n(k_TR)}{Y_n(k_TRi)}$$

References

[1] Abraham O, Dérobert X. Non-destructive testing of fired tunnel walls: the Mont-Blanc Tunnel case study. Int J Nondestruct Testing Eval 2003;36:411–8.
[2] Abraham O, Chammas R, Cote Ph, Pedersen HA, Semblat J-F. Mechanical characterisation of heterogeneous soils with surface waves: experimental validation on reduced-scale physical models. EAGE J Near Surf Geophys 2004;2(4):249–58.
[3] Aldrin JC. Models and classification procedures for ultrasonic inspection of holes for fatigue cracks. PhD thesis, North Western University, 2001.
[4] Aki T, Richards PG. Quantitative seismology: theory and methods, 2 vols. Freeman; 1980.
[5] Bodet L, vanWijk K, Bitri A, Abraham O, Côte Ph, Grandjean G, et al. Surface-wave inversion limitations from laser-Doppler physical modelling. J Environ Eng Geophys 2005;10(2):151–62.
[6] Breysse D, Abraham O. Méthodologie d'évaluation non destructive de l'état d'altération des ouvrages en béton. France: Presse des Ponts et Chaussées; 2005. 555p, ISBN 2 85978 405 5.
[7] Bungey JH, Millard SG. Testing of concrete in structures. Chapman & Hall; 1996.
[8] Chammas R, Abraham O, Côte Ph, Pedersen HA, Semblat J-F. Characterization of heterogeneous soils using surface waves: homogenisation and numerical modeling. ASCE Int J Geomech 2003;3(1):5–63.
[9] Epstein HI. The effect of curvature on Stoneley waves. J Sound Vibr 1976;46(1):59–66.
[10] Fong J, Lowe MJS, Gridin D, Craster RV. Fast technique for calculating dispersion relations of circumferential waves in annular structure. Rev Quant NDE 2003;22:213–20.
[11] Foti S. Multistation methods for geotechnical characterization using surface waves. PhD thesis, Politecnico di Torino, 2000. 299pp.

[12] Foti S, Sambuelli L, Socco LV, Strobbia C. Experiment of joint acquisition of seismic refraction and surface wave data. EAGE J Near Surf Geophys 2003;1:119–29.
[13] Graf KF. Wave motion in elastic solids. Dover publications; 1975.
[14] Gridin D, Craster RV, Fong J, Lowe MJS, Beard M. The high frequency asymptotic analysis of guided waves in a circular elastic annulus. Wave Motion 2003;38:67–90.
[15] Gucunski N,, Ganji V,, Maher MH. Effect of soil nonhomogeneity on sasw testing. Uncertainty in the geologic environment: from theory to practice, vol. 58. Geotechnical Special Publication; 1996. p. 1083–97.
[16] Hévin G, Abraham O, Pedersen HA, Campillo M. Characterisation of surface cracks with Rayleigh waves: a numerical model. Int J Nondestruct Testing Eval 1998;31(4):289–97.
[17] Jongmans D, Demanet D. The importance of surface waves in vibration study and the use of Rayleigh waves for estimating the dynamic characteristics of soils. Eng Geol 1993;34:105–13.
[18] Knopoff L. A matrix method for elastic wave problem. Bull Seismol Soc Am 1964;54:431–8.
[19] Leparoux D, Grandjean G, Bitri A. Underground cavity detection: a new method based on seismic Rayleigh waves. Europ J Environ Eng Geophys 2000;5:33–53.
[20] Lowe MJS. Plate waves for the NDT of diffusion bonded titanium. PhD thesis, Imperial College of Science, University of London, 1992.
[21] Lozier D, Olver F. Numerical evaluations of special functions. In: Proceedings of the AMS symposia in Applied Mechanics. 1994. p. 79–125.
[22] Lozier D. Software needs in special function. J Comput Appl Math 1996;66:345–58.
[23] Miller GF, Pursey H. On the partition of energy between elastic waves in a semi-infinite solid. Proc Roy Soc London 1955;233:55–69.
[24] Mokhtar TA, Herrmann RB, Russel DR. Seismic velocity and Q model for the shallow structure of the Arabian shield from short-period Rayleigh waves. Geophysics 1988;53:1379–87.
[25] O'Neil A. Full-waveform reflectivity for modelling, inversion and appraisal of seismic surface wave dispersion in shallow site investigations. PhD thesis, The University of Western Australia, Scholl of Earth and Geographical Sciences, 2003.
[26] O'Neill A, Matsuoka T. Some mode-misidentification pitfalls associated with discontinuous Rayleigh wave dispersion curves. J Environ Eng Geophys 2005;10(2).
[27] Park CB, Miller RD, Xia J. Multichannel analysis of surface waves. Geophysics 1999;64(3):800–8.
[28] Rayleigh JWS. On waves propagated along the plane surface of an elastic solid. Proc London Math Soc 1887;17:4–11.
[29] Ryden N, Park CB, Ulriksen P, Miller RD. Multimodal approach to seismic pavement testing. ASCE J Geotech Geoenviron Eng 2004;130:636–45.
[30] Ryden N, Lowe MJS. Guided wave propagation in three layer pavement structures. J Acoust Soc Am 2004;116(5):2902–13.
[31] Russel DR. Multi-channel processing of dispersed surface waves. PhD thesis, Saint Louis University, USA, 1987.
[32] Song WJ, Popovics JS, Aldrin JC, Shah SP. Measurement of surface wave transmission coefficient across surface-breaking cracks and notches in concrete. J Acoust Soc Am 2003;113(2).
[33] Sheriff RE, Geldart LP. Exploration seismology. 2nd ed. Cambridge University Press; 1995.
[34] Shtivelman V. Shallow water seismic survey for site investigation in the Haifa Port Extension area, Israel. J Appl Geophys 2001;46:143–58.
[35] Towfighi S, Kundu T, Ehsani M. Elastic wave propagation in circumferential direction in anisotropic curved plates. J Appl Mech 2002;69:283–91.
[36] Viktorov IA. Rayleigh and Lamb waves: physical theory and applications. Plenum Press; 1967.
[37] Xia J, Miller RD, Park CB. Estimation of near-surface shear-wave velocity by inversion of Rayleigh wave. Geophysics 1999;64:691–700.